

Stacking Order Regulated Coherent Shear Phonons in Octahedral MoTe₂ Revealed by Ultrafast Electron Microscopy

Wenli Gao, Shuaishuai Sun,* Yongzhao Zhang, Kaixin Zhu, Wentao Wang, Dong Yang, Jun Li, Huanfang Tian, Huaixin Yang, Xinghua Li, and Jianqi Li*



Cite This: *ACS Nano* 2025, 19, 19622–19634



Read Online

ACCESS |

Metrics & More

Article Recommendations

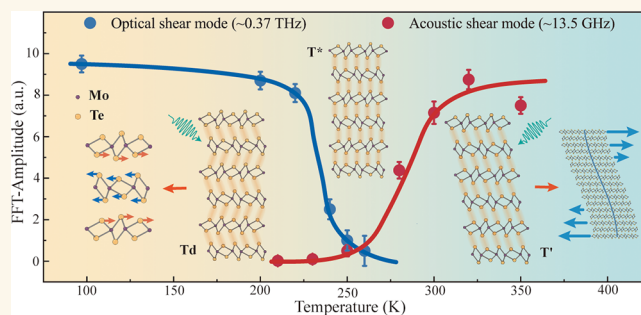
Supporting Information

ABSTRACT: Manipulation of the stacking order between layers in two-dimensional layered van der Waals materials provides a fascinating platform for exploring exotic phenomena. Femtosecond laser offers the capability to instantaneously modulate the lattice structure and even stacking order of layered materials, and vice versa, changes in stacking order may affect ultrafast structural dynamics. Here, we use ultrafast electron microscopy (UEM) to investigate the laser-excited lattice dynamics in T' and Td phases of octahedral MoTe₂. Two crystal plane-dependent acoustic phonon modes in the room temperature T' phase are identified by ultrafast selected-area electron diffraction (SAED) in reciprocal space and confirmed by ultrafast real-space imaging, which are attributed to the breathing mode and shear mode, respectively. Temperature-dependent ultrafast SAED results directly indicate that the acoustic shear mode switches to the optical shear mode when the stacking order is changed by crossing the phase transition temperature. Based on simple model derivations, shear acoustic waves in principle can be excited by the thermal elastic effect in low-symmetric 2D layered materials. However, incorporating numerical calculations and model analysis, we speculate that the laser-induced inverse piezoelectric effect plays a key role in the large-amplitude shear phonons observed in T'-MoTe₂. Our research demonstrates examples of stacking sequence identification using coherent phonons revealed by UEM, as well as the regulation of coherent shear phonons and topology switching via stacking order.

KEYWORDS: ultrafast electron microscopy, MoTe₂, shear mode, coherent phonon, stacking order, polarization bond

In two-dimensional layered van der Waals (vdW) materials, electronic properties can be modified by controlling the stacking sequence^{1,2} or twist angle between layers, which gives rise to a variety of novel quantum phenomena. Typical examples include unconventional superconductivity in twisted bilayer graphene,³ pressure tuning of magnetic order in CrI₃,⁴ emergent ferroelectricity in hexagonal boron nitride,^{5,6} and stacking-dependent topological phase.^{1,7,8} It is intriguing to utilize external perturbations to achieve stacking order switching, such as electric field,² optical field,^{9,10} and mechanical force.¹¹ Using femtosecond laser pulses to induce lattice strain and generate coherent phonons in nanofilms, including coherent optical phonons (COPs) and coherent acoustic phonons (CAPs),^{12–14} provides an important means to achieve ultrafast control of physical properties related to stacking order.¹⁵

COPs primarily promote the relative motion of atoms within a unit cell, inducing the precursor of a phase transition or



directly switching the topological state. The frequency range of optical phonons covers ~0.1–10 THz and is typically characterized using Raman spectroscopy.^{16,17} In contrast, CAPs are associated with the collective motion of atoms across unit cells, where the phonons vibrate at frequencies in the gigahertz range and can be observed using ultrafast pump–probe techniques.^{18–21} In this paper, only CAPs propagating along the surface normal direction (i.e., *c** direction) of a film are considered, which are resonantly enhanced and manifest as a standing wave due to constructive interference between the

Received: December 10, 2024

Revised: May 7, 2025

Accepted: May 7, 2025

Published: May 16, 2025



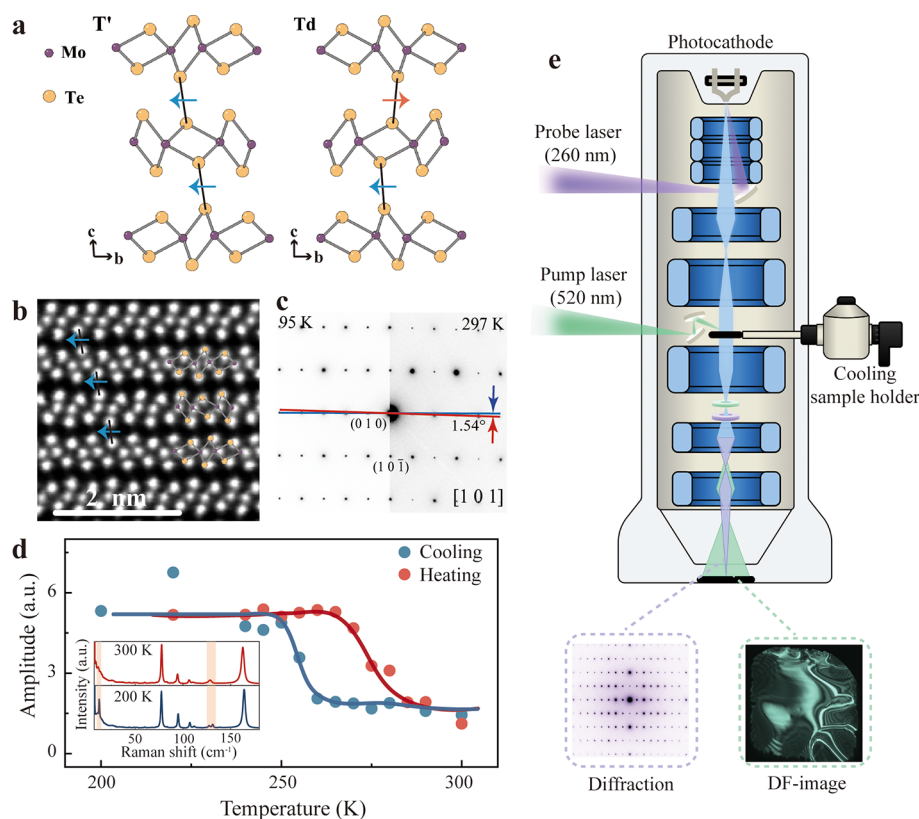


Figure 1. Temperature-driven structural phase transition of MoTe₂ and schematic of a cryogenic UEM. (a) Schematics of MoTe₂ crystal structure in the monoclinic T' phase and orthorhombic Td phase. The two phases have the same in-plane structure but different vertical stacking sequence. (b) Cross-sectional atomic-resolution STEM imaging of T'-MoTe₂ at room temperature, overlaid with the schematic diagram of atomic structure. The black lines connect the Te–Te atom pairs of the two layers, while the blue arrows indicate the displacement between the adjacent monolayers. (c) SAED patterns along [101] acquired at 97 (left) and 297 K (right) display an angle difference of about 1.5° between the (010) and (101) diffraction peaks. (d) Temperature-dependent intensity evolution of low-frequency Raman peak (~12 cm⁻¹). Inset shows two typical Raman spectrum at 200 and 300 K. (e) Schematic diagram of cryogenic UEM setup, showing both the imaging mode and diffraction mode with green and purple encoded electron beam traces, respectively.

top and bottom surface reflected waves.¹⁴ Based on their polarization direction, the CAPs propagating along the c^* direction can be categorized into two distinct modes: the out-of-plane breathing mode (longitudinal acoustic, LA),²² which is polarized along the c^* direction and can be conventionally excited in thin films, and the in-plane shear mode (transverse acoustic, TA)²³ polarized along the a -axis or b -axis, whose excitation conditions are relatively strict. The excitation of TA shear mode remains challenging in high-symmetry systems^{24–26} and has only been demonstrated in very few low-symmetry systems.^{19,27–29}

Due to rich physical properties, in particular the diverse topological phases related to stacking sequence, transition-metal dichalcogenide (TMD) MoTe₂ have attracted great attention.^{1,9,15,16,21,30–38} Compared with the trigonal prismatic 2H phase, distorted octahedral MoTe₂ undergoes a first-order structural phase transition from the centrosymmetric monoclinic T' to a noncentrosymmetric orthorhombic Td phase at a transition temperature (T_c) of ~250 K.³⁹ Figure 1a illustrates the atomic structure diagram of MoTe₂ in the bc -plane. The left side is the T' phase with a monoclinic angle α of 93.75° (in this paper, we define $a = 3.47$ Å, $b = 6.34$ Å), and the right side is the Td phase. It can be seen from the figure that the in-plane monolayer Mo atomic chains display a Peierls distortion, driving the out-of-plane folding of Te atoms. The T' and Td phases exhibit distinct interlayer slip along the b axis

corresponding to different stacking orders. The Te atoms in each layer slip in a single direction in the T' phase (blue arrow), while alternately changing direction in the Td phase (blue and orange arrows). Subtle changes in structure related to stacking order have been achieved by ultrafast laser excitation over a wide range of wavelength, realizing a topological electronic transition from Weyl semimetal (Td phase) to topological trivial state³¹ through interlayer shear displacements across a metastable intermediate T* state,^{9,15,33,34} offering great potential for ultrafast topological control^{15,32} and optoelectronic switching. Furthermore, understanding the dynamic behavior of the T' phase under laser excitation, which is also governed by interlayer slip, and exploring the similarities in the dynamic processes of the two phases could advance the development of slidetronics.

We have observed laser-excited coherent strain waves in high-symmetry 2H-MoTe₂ by ultrafast selected-area electron diffraction (SAED) in our previous work.²⁶ Only the breathing mode with a single oscillation frequency was found in the very thin flake, while the high harmonics started to emerge beyond a critical thickness of ~40 nm due to the inhomogeneous excitation along the depth direction. Here, we use ultrafast electron microscopy (UEM) to determine the response of coherent shear phonons in distorted octahedral MoTe₂ under ultrafast laser excitation. The existence of acoustic shear phonons in room temperature monoclinic T'-MoTe₂ was

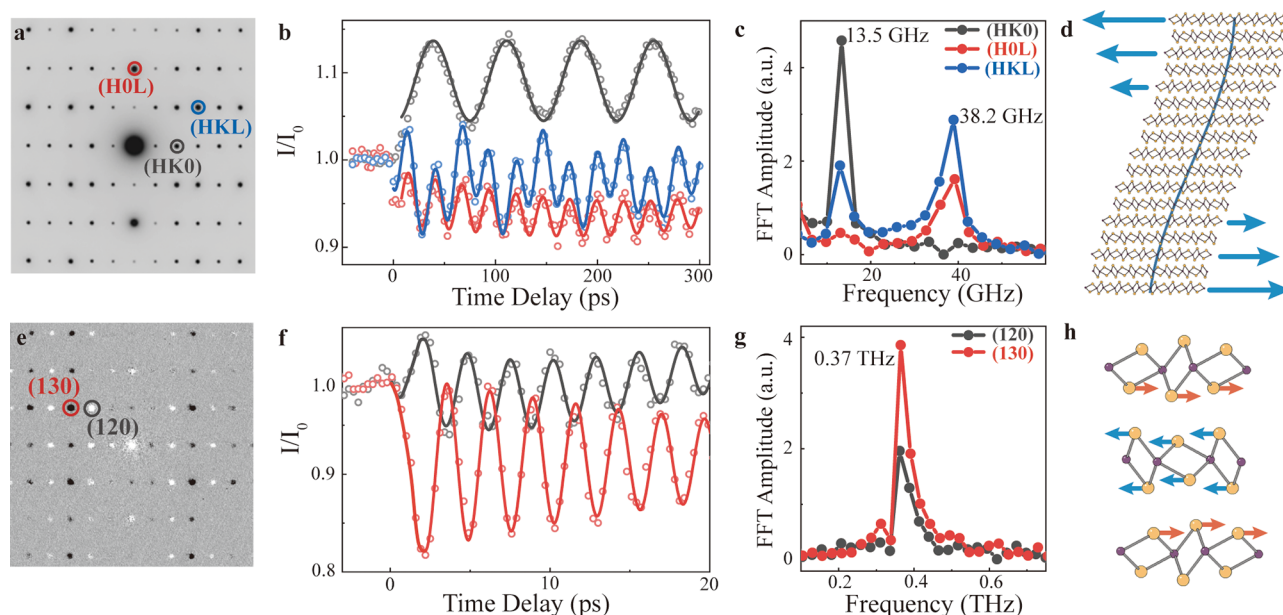


Figure 2. Identification of different phonon modes by ultrafast electron diffraction. (a) SAED of MoTe₂ in the room temperature (~ 297 K) T' phase along the [0kl] zone axis. (b, c) Laser-induced intensity changes (b) and corresponded fast Fourier transformation (FFT) amplitudes (c) of diffraction peaks as color coded in (a). (HK0), (H0L), and (HKL) correspond to $(\bar{1}20)$, (204) and $(11\bar{2})$, respectively. The two crystal plane-dependent frequency components were attributed to acoustic breathing mode (38.2 GHz) and shear mode (13.5 GHz). (e) SAED difference map of MoTe₂ in the low-temperature (~ 97 K) Td phase along the [001] zone axis, i.e., a plot of the difference between the peak and valley time delay. (f, g) Laser-induced intensity changes (f) and corresponding FFT amplitudes (g) of diffraction peaks as color coded in (e). The ~ 0.37 THz oscillation reflects the optical shear phonon mode. (d, h) Schematic diagram of acoustic (d) and optical (h) shear phonons. Experiments were conducted on area #1 with a pump fluence of 0.5 mJ/cm².

confirmed by both ultrafast SAED and ultrafast dark-field (DF) imaging, with the evidence that the acoustic phonon mode was related to specific crystal plane indices. The temperature dependence of the coherent shear phonon modes was directly observed by temperature-dependent ultrafast SAED experiments, and the results show that the acoustic shear mode and optical shear mode along the same direction exist in the T' and Td phases, respectively. Combined with the quantitative determination of shear wave amplitude and numerical simulation of elastic wave equation, within the framework of the interlayer bond polarizability model, we speculate that the key driving force of acoustic shear phonon modes was stacking order-related inverse piezoelectric effect.

RESULTS AND DISCUSSION

Stacking Order of MoTe₂ and Temperature-Driven Structural Transition. In order to directly determine the stacking order and atomic structure of our MoTe₂ sample, we performed room temperature high-angle annular dark-field (HAADF) scanning transmission electron microscopy (STEM) imaging of cross-sectional samples (*bc*-plane) prepared by using focused ion beam (FIB). The STEM image with the overlaid crystal structure diagram shown in Figure 1b directly demonstrates the Mo atom dimerization, Te atom folding, and monoclinic structure of MoTe₂, where the blue arrow represents the direction of slip between adjacent layers. Further analysis of the T'-MoTe₂ interlayer stacking structure shows that the interlayer slip direction can have a twin variant,³⁵ as shown in Figure S1c,e. The monoclinic angle would be extracted directly from the electron diffraction pattern in the *bc*-plane (see Figure S1b,d), which is the most suitable parameter for monitoring the temperature-driven structural phase transition. However, the observed monoclinic

angle did not change when the sample was cooled to far below the reported T_c . A similar situation has been encountered in the previous report using the same preparation method,¹ which was attributed to the mechanical restriction of layer sliding by the outer amorphous layer created during the sample preparation.

We further performed temperature-dependent SAED along the [101] direction in mechanically exfoliated *ab*-plane thin flakes by tilting the sample $\sim 14^\circ$ away from the surface normal. The SAED patterns (Figure 1c) at low temperature (97 K) and room temperature (297 K) show an angular change of approximately 1.5° between the (010) and $(10\bar{1})$ diffraction peaks, indicating that a structural phase transition occurred in the exfoliated sample. Temperature-dependent Raman scattering measurements were also conducted to confirm the interlayer stacking structural phase transition. The inset of Figure 1d shows two Raman spectra acquired at 300 and 200 K. A new peak located at 12 cm^{-1} (corresponding to the 0.37 THz interlayer shear mode) emerged at 200 K due to the inversion symmetry breaking.^{36,37} The intensity of this characteristic peak was used to quantify the phase changes, showing a transition near the temperature of 265 K with a hysteresis range of ~ 15 K (more details can be found in Section 2 of the Supporting Information).

Excitation of Coherent Shear Phonon Revealed by Ultrafast SAED. The sample used for ultrafast SAED is placed on a 2000 mesh copper grid using a mechanical exfoliation technique, and the thickness was measured to be 18.6 ± 3.7 nm (see Figure S3, area #1). A typical SAED pattern of T'-MoTe₂ at room temperature is shown in Figure 2a. A 300 fs, 0.55 mJ/cm² laser with a wavelength of 520 nm was employed to excite a free-standing thin flake, which was tilted to a specific zone axis. The intensity changes as a function of time for each

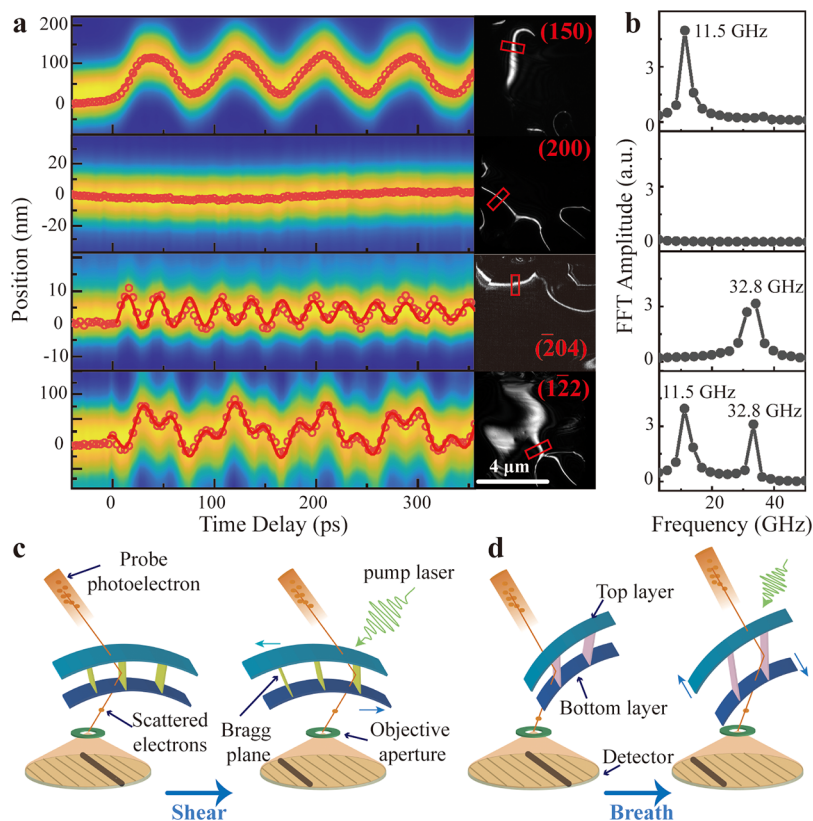


Figure 3. Direct observation of the acoustic standing wave by ultrafast DF imaging. (a) Laser-induced bend contour movement in DF images (right column), which were formed by selection of different diffraction peaks. Each color map is constructed by the line scan along the long side of the red rectangle at different time delays. The red open circle on the top of color map is obtained by Gaussian fitting the line scan of bend contour at each time delay, and the red solid line is the fitted curve by sine wave function. (b) FFT amplitudes of the corresponded oscillating data in (a). (c, d) Schematic diagram showing how the shear (c) and breathing (d) motions can affect the bend contour position in DF images. Experiments were conducted on area #2 with a pump fluence of 0.5 mJ/cm^2 .

diffraction peak are shown in Figure 2b, and two oscillation frequencies can be distinguished from these intensity oscillations (Figure 2c). The extracted frequency was found to be $\sim 13.5 \text{ GHz}$ for the Bragg peaks with Miller index containing the K-component (black curve in Figure 2b,c) and $\sim 38.2 \text{ GHz}$ for the one containing the L-component (red curve in Figure 2b,c). Diffraction peaks containing K and L components show coupled oscillations (blue curves in Figure 2b,c). Several more samples with variable thickness and substrate have been checked. The two frequency components have been observed for all of the samples, with slightly different values for each component but almost the same ratio (~ 2.8) between higher and lower frequencies (Table S1). Recently, two vibration modes have been reported in Bi_2Se_3 by ultrafast X-ray diffraction.⁴⁰ The frequencies of both components display thickness dependency. The higher frequency is attributed to the breathing mode, while the lower frequency mode is attributed to the interface mode caused by the weak interaction between the film and substrate.⁴¹ However, the lower frequency we observed in $\text{T}'\text{-MoTe}_2$ cannot be attributed to the interface mode due to the fact that it has been found in both suspended and substrate samples.

In the continuous medium approximation, the fundamental oscillating frequency of standing acoustic waves can be calculated by $f = v/2d$, where d is the sample thickness and v is the acoustic wave velocity. Following the general definition of the elastic moduli matrix, we can relate acoustic phonon branch velocities to corresponding C_{ij} components by $C = \rho v^2$,

where ρ is the mass density.⁴² According to the elastic modulus of $\text{T}'\text{-MoTe}_2$,⁴³ the wave velocity for each acoustic branch is calculated to be $v_{\text{LA}[001]} \approx \sqrt{\frac{C_{33}}{\rho}} = 1.76 \text{ km/s}$,

$$v_{\text{TA}[100]} = \sqrt{\frac{C_{55}}{\rho}} = 1.9 \text{ km/s}, \quad \text{and}$$

$v_{\text{TA}[010]} \approx \sqrt{\frac{C_{44}}{\rho}} = 0.62 \text{ km/s}$. We note that the ratio (~ 2.84) of the sound velocity of $v_{\text{LA}[001]}$ and $v_{\text{TA}[010]}$ is consistent with that of the observed oscillation frequency. Recall the dependence of oscillation frequency on the crystal plane Miller index; we can naturally attribute the oscillation frequency of 38.2 GHz to the breathing mode and the one of 13.5 GHz to the in-plane shear mode along the b axis (monoclinic direction, as shown in Figure 2d). The acoustic shear wave has also been observed in VTe_2 , which is associated with optically induced CDW dissolution and displays a threshold effect.⁴⁴ However, the fluence dependence data in $\text{T}'\text{-MoTe}_2$ (Figure S4a–d) show a linear relationship, implying a different excitation mechanism.

When the sample was cooled to 97 K , the acoustic shear modes disappeared; in the meantime, intensity oscillation of all Bragg peaks with a frequency of $\sim 0.37 \text{ THz}$ was detected. The oscillation curves of two typical Bragg peaks (120) and (130) are shown in Figure 2f. The extracted frequency in Figure 2g is consistent with the measured Raman peak (12 cm^{-1} , Figure 1d and Figure S2) and previous reported interlayer optical shear phonons,^{15,32,45,46} in which atoms in the same layer move in

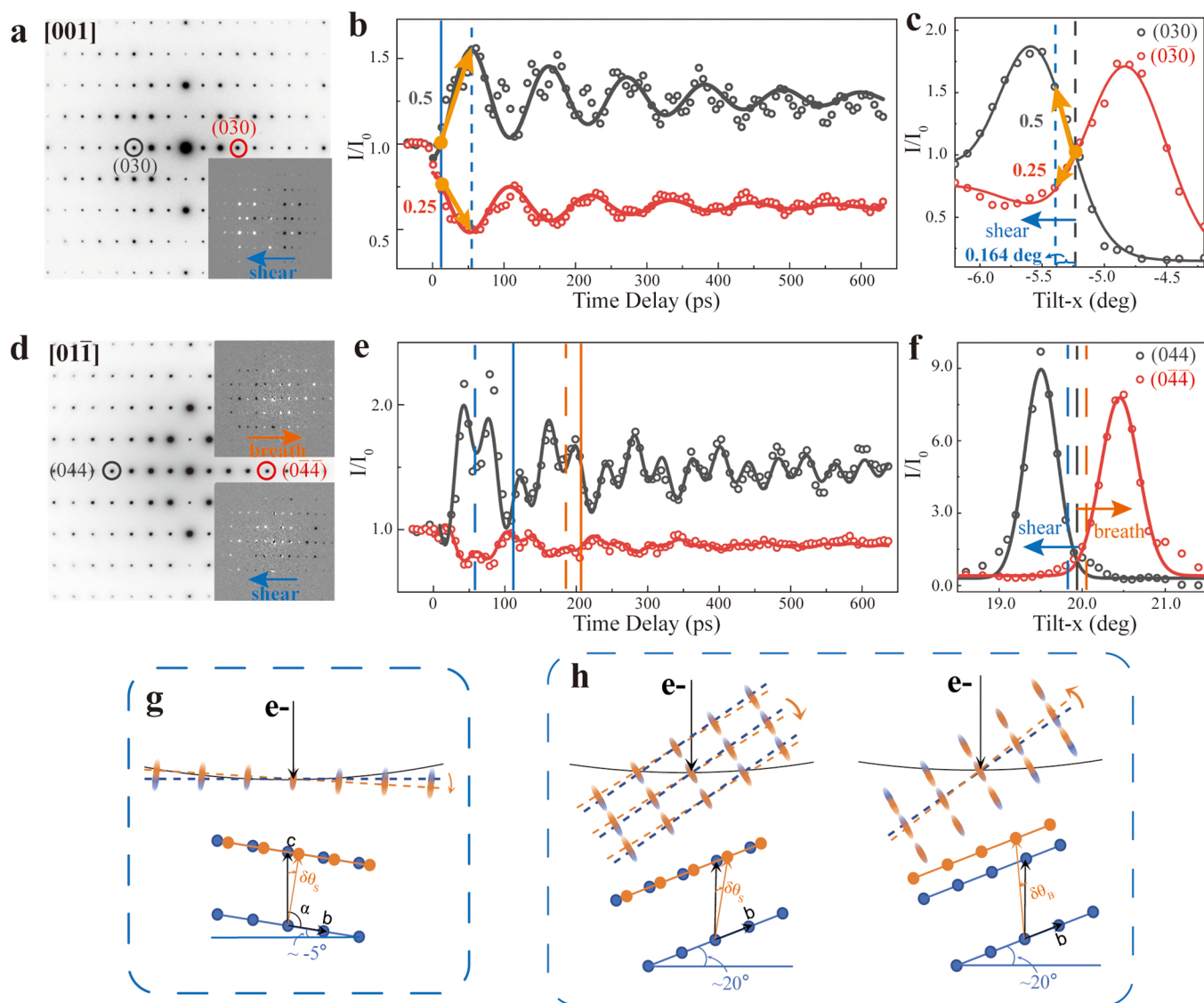


Figure 4. Quantitative characterization of acoustic motion. (a, d) Experimental diffraction patterns along the $[001]$ and $[01\bar{1}]$ zone axis; inset is the difference map between delay points of peak and valley for the corresponding mode. (b, e) Intensity changes of color-coded Bragg peaks in (a, d). The solid and dashed vertical lines mark the delay points for the difference map. (c, f) Rocking curve of Friedel pairs by tilting the sample along the b axis. The ultrafast experiments were performed at the tilt angle marked by the black dashed vertical line. The arrow indicates the virtue tilting direction caused by acoustic phonon as depicted in (g) and (h). The lower and upper panels of (g) and (h) schematically illustrate the atomic displacements and associated reciprocal space tilt, respectively. The blue dot represents the initial position and the orange dot represents the position after laser excitation considering only one acoustic mode. The sample was supported on a 30 nm-thick Si_3N_4 window to obtain a relatively flat surface. Experiments were conducted on area #3 with a pump fluence of $1.3 \text{ mJ}/\text{cm}^2$.

the same direction along the b axis (monoclinic direction), while atoms in adjacent layers move in the opposite direction, as illustrated in Figure 2h. The topological properties of the Td-phase MoTe_2 can be changed by the optical shear phonons, and the material will undergo an electronic phase transition from topological to a trivial semimetal, realizing the photo-induced topological switch.^{15,32} The generation of 0.37 THz optical shear phonon in Td- MoTe_2 has been attributed to the mechanism of dispersive excitation of coherent phonons^{9,47} (DECP), which alter the intensity of the diffraction peak primarily by modifying the structure factor within the unit cell. This can be verified from the difference in the diffraction pattern between the peak and valley time delay, as shown in Figure 2e. The Bragg peaks with the same K components have the same black or white color, indicating that their intensities

oscillate with the same phase. This optical shear mode was significantly softened when using higher pump fluence (see Figures S4e,f and S9c).

Direct Visualization of Acoustic Standing Wave by Ultrafast DF Imaging. In addition to the averaged atomic structure displacement obtained by ultrafast SAED in reciprocal space, the localized structure movement with spatial variation can be directly ascertained through the utilization of UEM imaging mode in real space with an adequate level of magnification, which may reflect such as anisotropic morphological dynamics⁴⁸ and the impact of defects on the generation and propagation of strain waves.^{49–51} The DF imaging in UEM (DF-UEM), which uses scattered electrons with specific vectors through the objective aperture to form an image, can facilitate a more convenient verification of the

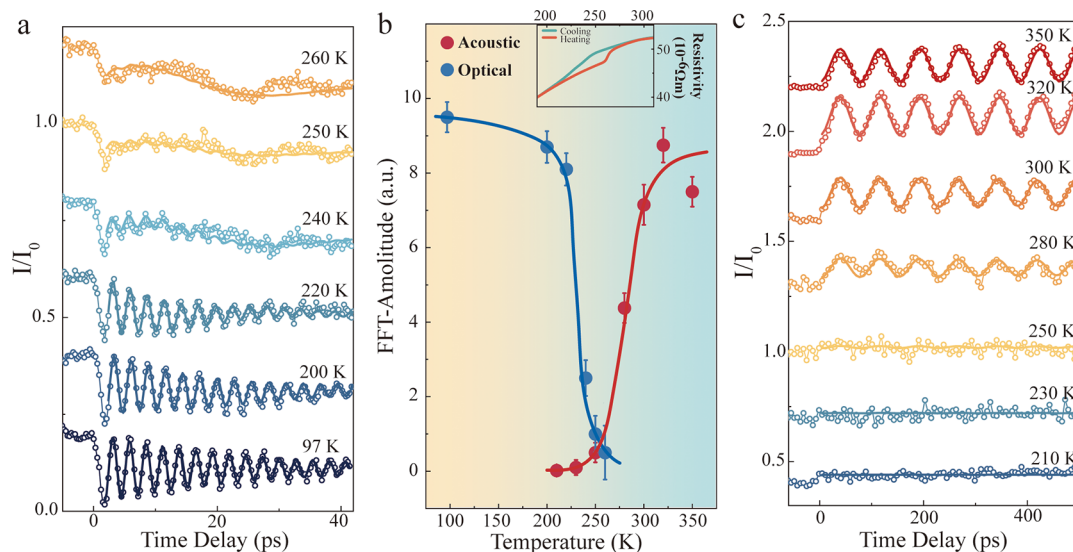


Figure 5. Temperature-dependent shear mode transition. (a, c) Laser-induced intensity oscillations of (130) (a) and ($\bar{1}20$) (c) peaks acquired at different temperatures. The oscillations in (a) and (c) correspond to optical and acoustic shear phonons with the frequency of 0.37 THz and 13.5 GHz, respectively. (b) Oscillation amplitudes of optical and acoustic shear phonons as a function of temperature, displaying a clear transition temperature around 250 K which overlaps well with the electrical transport data (inset). Curves in parts (a) and (c) are vertically offset for visual clarity. Experiments were conducted on area #1 with a pump fluence of 0.5 mJ/cm².

dependence of acoustic waves on a certain crystal plane index. The DF-UEM has been used to image vibrational dynamics of nanoparticles⁵² and order parameter evolution of light-induced CDW phase transition.⁵³ Although the real-space imaging is better suited to investigate the spatial heterogeneity impact on phonon dynamics, here we use DF-UEM to focus on the distinguishing acoustic wave dynamics associated with specific Bragg peaks to confirm the identification of shear and breathing modes.

The sample used for DF-UEM is suspended on a 2000 mesh copper grid and naturally has a relatively large curved shape. The thickness was 23.1 ± 4.6 nm (see Figure S3, area #2). We selected different diffraction peaks in the same region on the free-standing sample to generate the DF image, as shown in the right panel of Figure 3a and Figure S5. The left panel of Figure 3a plots the bend contour shift with respect to the time delay after pump laser excitation (see Videos S2–S5), integrated along the long side of the red rectangle in the right panel of Figure 3a. The red circle overlaid on the top of the 2D map represents the fitted center position of the bend contour, which also demonstrates the Miller index-dependent oscillation similar to diffraction intensity. The corresponding FFT results are shown in Figure 3b, where the extracted frequency consists of the oscillation frequency of diffraction intensity revealed by ultrafast SAED (Figure S6). It can be seen that the bend contour with $K \neq 0$ (150 and $\bar{1}22$) has an oscillation with 11.2 GHz component, the one with $L \neq 0$ ($\bar{2}04$ and $\bar{1}22$) has a 32.5 GHz component, whereas the one with $K, L = 0$ (200) shows no oscillation. This further confirms the dependence of different coherent acoustic modes on specific crystal plane indices.

Before pump laser excitation, the electron beam is scattered by crystal planes satisfying specific Bragg diffraction, and forms a bright bend contour on the detector through the selection of the objective lens aperture⁵⁴ (as shown on the left panel of Figure 3c,d). Both the acoustic shear phonon and breathing phonon can cause the oscillation of the bend contour position, but the underlying mechanism is different. The standing wave

of acoustic shear phonon causes the top layer and bottom layer move transversely (along in-plane direction) in the opposite direction, and the acoustic breathing phonons mainly regulate the top layer and bottom layer expand or contract vertically (along out-of-plane direction) in the opposite direction, as marked by the blue arrows in the right panel of Figure 3c,d respectively, resulting in a change of the spatial position where the crystal plane satisfies Bragg diffraction, and thus the curved contour fringe on the detector moves accordingly. It is worth noting that the curved shape of the thin flake significantly magnifies the real atomic movement, as encoded in the bend contour shift.

Quantitative Determination of Shear Strain. Ultrafast DF imaging data from curved samples demonstrate the visualization of the acoustic phonons with a fantastic signal-to-noise ratio, but it is a challenge to quantify the amplitude of phonons through the bend contour movement due to their high sensitivity to the local curvature, which is very difficult to determine. In order to obtain the movement direction and amplitude of coherent acoustic phonons, we further performed ultrafast SAED experiments on a rather flat sample supported by Si₃N₄ substrate (see Figure S3, area #3), under an excitation fluence of 1.3 mJ/cm². The diffraction intensity evolutions of Friedel pairs under different zone axes were quantitatively analyzed and compared with the rocking curve of the corresponding peaks.

Figure 4 shows the ultrafast SAED data acquired at the $[001]$ and $[01\bar{1}]$ zone axes (see more data at other zone axes in Figure S7). The diffraction intensity of (030) and $(0\bar{3}0)$ in Figure 4b displays an antiphase oscillation after time zero. As is well-known, the coherent acoustic phonons facilitate the collective movement of atoms across unit cells in the film, which subsequently alters the intersection position between the reciprocal rod and the Ewald sphere.²⁷ This is ultimately manifested in the change of the diffraction peak intensity.⁵⁵ The sign and amplitude of the change highly depend on the deviation of the incidence direction and zone axis, which is related to the tilt angle. If the sample is under zone axis

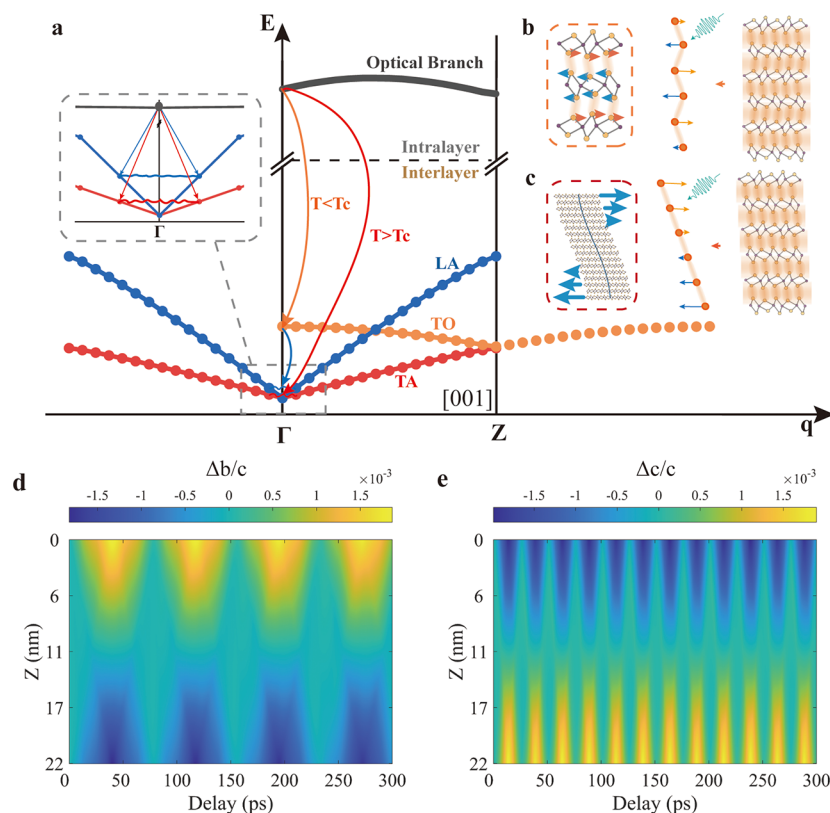


Figure 6. Schematic diagram of phonon scattering paths and simulated atomic displacements. (a) Illustration of the dominant intralayer optical to interlayer TO (then to LA, blue arrow) or TA scattering pathways below (orange arrow) and above (red arrow) the transition temperature. The schematic on the left shows two acoustic phonons with opposite wave vectors couple together to form standing wave at the Γ point. (b, c) Schematic of the interlayer polarization bond and related shear motion. The orange shaded area in the right panel represents the electric dipole due to the charge accumulated in the weak interlayer covalent bonds. The central panel shows an exaggerated view of the interlayer bond orientations between different layers and demonstrates the collective motion of the layers along the directions indicated by the arrows, driven by the dipole moments under laser excitation. This motion manifests as the atomic displacements associated with the two phonon modes depicted in the left panel. (d, e) Simulation of atomic displacement in a 22 nm-thick free-standing sample with laser fluence of 1.3 mJ/cm^2 , showing the propagating of shear mode (d) and breathing mode (e) phonons along the z (r_3) direction.

excitation, which is our experimental condition, the intensity of Friedel pairs will change oppositely under the modulation of acoustic phonons (Figure 4g,h). As we can see in the difference map between the oscillation peak and valley delay points (inset of Figure 4a), the intensity changes of almost all Friedel pairs manifest opposite trends, where the left part became stronger, and the right part became weaker. The symmetry of the difference map reflects that the virtual tilt of reciprocal space caused by the acoustic phonons is along the b direction. The sample is then rotated so that the tilt direction of goniometer is along the b axis, and the rocking curve of certain Bragg Peak is obtained by extracting the diffraction intensity of a series of continuously tilted diffraction pattern, as shown in Figure 4c. By comparison of the intensity change in ultrafast data and rocking curves of (030) and (0 $\bar{3}$ 0), indicated by the yellow arrows in Figure 4b,c, we can speculate that the acoustic shear phonon caused a virtual tilt of $\delta\theta_{[001]\text{shear}} = \delta\theta_s = 0.164^\circ$ toward a more orthogonal direction. Through the triangular relationship, we can get the shear amplitude of $\frac{\Delta b}{c} = \delta\theta_s \times \frac{\sin \alpha}{\cos^2 \theta_s}$ is $\sim 2.9\%$, where $\theta_s = -4.4^\circ$ is the angle between the view direction (electron beam incident) and c^* direction (more details can be found in Section 8 of the Supporting Information).

In order to extract the breathing amplitude, we perform ultrafast SAED experiments under the $[01\bar{1}]$ zone axis and

analyze the diffraction intensity of (044) and (0 $\bar{4}$ 4) shown in Figure 4e, exhibiting coupled oscillations related to both breathing and shear acoustic phonons. By looking into the difference map and rocking curves, we can see that the virtual tilt direction caused by shear and breathing phonons is opposite. The cartoon in Figure 4h explains the reverse tilt direction caused by two types of layer motion. The breathing amplitude is calculated to be $\frac{\Delta c}{c} = \delta\theta_B \times \frac{2}{\sin 2\theta_B} = 3.2\%$ toward expansion direction, where $\delta\theta_{[01\bar{1}]\text{breathing}} = \delta\theta_B = 0.060^\circ$ is the virtual tilt angle by breathing mode, $\theta_B = 70^\circ$ is the angle between view direction and b axis.

Temperature Dependence of Shear Modes. In ultrafast SAED experiments, we already demonstrated that optical shear phonons with a characteristic frequency of about 0.37 THz are generated in MoTe_2 under low-temperature laser excitation, whereas acoustic shear phonons in the GHz range are mainly generated at room temperature. To explore the relationship between these two modes, temperature-dependent ultrafast SAED experiments were performed. Figure 5a (light-colored circles) illustrates the intensity oscillations of (130) peaks acquired at different temperatures, showing that the oscillation amplitude of optical shear phonon mode progressively diminishes with increasing temperature, accompanied by the emergence of other low-frequency oscillations at 240 K. Notably, the high-frequency optical shear phonons exhibit

discernible frequency shifts and lifetime variations at 97 and 200 K. Quantitative analysis using damped sine function fitting (solid curves in Figure 5a) yields key parameters including oscillation amplitudes (blue points in Figure 5b), frequency shifts, and damping constants (Figure S9). The observed progressive frequency softening originates from thermally activated phonon decay processes, where optical phonons decay into more phonon modes, thereby enhancing lattice anharmonicity and inducing frequency reduction.⁵⁶ Furthermore, the accelerated frequency softening near 250 K correlates with the progressive disappearance of optical phonon modes. Concurrently, the vibration amplitude and damping constant of optical shear phonons exhibit trends similar to those observed in frequency, providing additional evidence for the disappearance of these phonons near 250 K. In contrast, the (120) diffraction peak analysis (Figure 5c, light circles) reveals that as the temperature further increases, the acoustic shear phonons emerge and gradually reach saturation at around 300 K. The amplitude of the acoustic shear oscillation (red points in Figure 5b) was extracted from the fitted sine function (solid curves in Figure 5c). Ultimately, the oscillation amplitudes of these shear phonon modes as a function of temperature are summarized in Figure 5b. A clear transition between the two phonon modes occurs around 250 K, which coincides with the transition temperature of the resistance curve and is consistent with the reported T_c in previous literature.^{36,39} This strong correlation between the shear phonon mode and the transition temperature provides a reliable fingerprint for characterizing the structural phase transition in MoTe₂. The results indicate that temperature drives a change in the interlayer stacking sequence of the octahedral MoTe₂, subsequently altering the photoinduced coherent shear phonon modes. This highlights the fundamental role of shear phonons in tracking structural dynamics during phase transitions.

Possible Driving Force of Acoustic Shear Wave. The above experimental results clearly demonstrated that acoustic shear phonons were excited in the high-temperature T' phase, while optical shear phonons were excited in the low-temperature Td phase, and both of them shear along the monoclinic direction. Recently, Cheon et al.³⁷ observed interlayer shear phonon modes with opposite trends of layer-dependent frequency evolution in few-layer Td- and T'-MoTe₂, respectively, through low-frequency Raman spectroscopy. The multiple low-frequency interlayer Raman modes, including shear and breathing modes, were extensively reported in few-layer two-dimensional materials, which have been used for determining layer numbers and even stacking order.

A simple linear chain model (LCM) was proposed to explain the multiple-layer-dependent Raman modes, which considers each layer as a rigid ball and interlayer coupling as a harmonic spring. The Eigenmodes of LCM⁵⁷ are $u_n^\alpha \propto \cos \frac{\alpha(2n-1)\pi}{2N}$ and the corresponding phonon frequencies $f_\alpha = \frac{1}{\pi} \sqrt{\frac{\beta}{m}} \sin \frac{\alpha\pi}{2N}$, where β is the interlayer force constant per unit area, m is the mass per unit area of each layer, n denotes the n -th layer, and $\alpha = 1, 2, \dots, N - 1$. When the layer number N is determined, the $\alpha = N - 1$ mode corresponds to the acoustic phonon close to the first Brillouin zone boundary, which can be folded back to the zone center as optical phonon when considering two layers in one unit cell (see the orange dots and

solid lines in Figure 6a),²³ and $\alpha = 1$ mode corresponds to the acoustic phonon near the Γ point (as shown in Figure 6a, the red spot close to the Γ point). When N is very large, f_1 can be approximated as $f_1 \approx \sqrt{\frac{\beta}{m}} \frac{1}{2N} = \sqrt{\frac{\beta t}{m/t}} \frac{1}{2Nt} = \sqrt{\frac{c}{\rho}} \frac{1}{2d} = \frac{v}{2d}$.

The standing waves with the frequency f_1 are formed by two propagating waves with the same frequency but opposite wave vectors coupling to the Γ point, as shown in the upper left inset of Figure 6a. The more than two orders of magnitude difference in frequency that we observed for the interlayer shear mode can then be unified by LCM with two extreme conditions. The low-temperature optical shear mode corresponds to the $\alpha = N - 1$ mode, where adjacent layer shear reversely, while the high-temperature acoustic shear mode corresponds to the $\alpha = 1$ mode, where the half cycle of one shear wave propagates across the whole film. The mechanisms of their arising in different types of MoTe₂ still need to be elucidated.

The reported Raman intensities of interlayer shear modes in few-layer films exhibit quite different trends depending on complex stacking sequences. As a general rule, the lowest frequency mode of AB-stacked sample (2H-TMD, NbSe₂, AB-stacked graphene) has the strongest Raman intensity and blue shift with increasing layer numbers, while the opposite trend is true for ABC-stacked sample (3R-TMD, Bi₂Se₃, ABC-stacked graphene), which is consistent with recent studies on MoTe₂.³⁷ An interlayer bond polarizability model^{57,58} has been proposed to explain and predict the stacking-dependent Raman intensity of low-frequency interlayer shear mode in layered materials, where the stacking sequence of nonperpendicular weak covalent character of interlayer interactions plays a key role. The charge accumulated in the weak covalent bond (see the orange area on the right panel of Figure 6b,c) produces dipole moments in the presence of the electric field of the pumping laser or the transient electric field created by the image potential state,⁵⁹ and further promotes interlayer vibrations. The interlayer polarization bond model can be understood as the reorientation of transient dipole moments in layered materials with weakly covalent character, driven by the electric fields of photocarriers. This mechanism is especially prominent in octahedrally distorted MoTe₂, which exhibits a relatively long lifetime of photocarriers.^{60,61} The middle part of Figure 6b,c enlarges the orientation of the electric dipole moments between adjacent layers in different phases of MoTe₂, and demonstrates the collective motion of each layer in the direction indicated by the arrow under the drive of the dipole moment with laser excitation. Based on transient dipole reorientation, MoTe₂ will transit toward a higher-symmetry T* phase along the direction of the transient electric field: adjacent layers should shear completely out-of-phase for Td-MoTe₂ ($\alpha = N - 1$ mode), while the whole film should be stretched out for T'-MoTe₂ ($\alpha = 1$ mode), as shown in the left inset of Figure 6b,c. In short, the phonon mode number α with the strongest vibration amplitude is directly linked to the stacking sequence, where the T' phase (ABC stacked) has the strongest intensity for the mode that $\alpha = 1$ (acoustic shear phonon), while the Td phase (AB stacked) has the strongest intensity for the mode that $\alpha = N - 1$ (optical shear phonon). In addition, the recently emerged sliding ferroelectricity⁶² in layered vdW materials, such as 1T'-ReS₂,⁶³ WTe₂,⁶⁴ and 3R-MoS₂,⁶⁵ highlights the close relationship between interlayer electron cloud transfer and interlayer sliding, which is consistent with the interlayer bond polarizability model.

Figure 6a summarizes the schematic phonon scattering paths following laser excitation. Upon laser excitation, valence electrons are instantaneously excited to the conduction band, initiating a cascade of electron–electron and electron–phonon interactions. Below T_c , the AB stacking sequence characteristic of the Td phase facilitates the scattering of intralayer optical phonons into interlayer optical shear phonons, which further decay into acoustic breathing phonons. When temperature (Figure 5a) or fluence (Figure S4e,f) increases, intralayer optical phonons tend to directly decay into the acoustic breathing phonons. Conversely, above T_c , the ABC stacking sequence of the T' phase drives the scattering of intralayer optical shear phonons into interlayer acoustic shear phonons.

In order to get a quantitative estimation of the shear and breathing amplitude to further clarify the possible driving force, the elastic wave equation is numerically solved to extract the atomic displacement (see Section 10 of the Supporting Information). The generation mechanisms of coherent acoustic phonons are well-documented¹² and primarily include the thermoelastic effect, lattice deformation potential, and inverse piezoelectric effect. Among these, the thermoelastic effect and lattice deformation potential are present in nearly all samples, but the latter exists for only a very short period of time (\sim ps). In the following simulation, the T'-MoTe₂ film is regarded as a one-dimensional continuous elastic medium, and only the photothermo stress due to thermoelastic effect is taken into account as the external source term. Then, the wave equation can be described as follows:

$$\rho \frac{\partial^2 u_i}{\partial t^2} = \sum_{j=1,2,3} \frac{\partial \sigma_{ij}}{\partial r_j}, \quad i = 1, 2, 3 \text{ or } x, y, z \quad (1)$$

$$\sigma_{ij} = \sum_{k,l=1,2,3} C_{ijkl} (\varepsilon_{kl} - \Delta T \times \beta_{kl}) \quad (2)$$

where ρ is the mass density, u_i is the i th component of the atomic displacement vector, C_{ijkl} is the elastic moduli matrix, σ_{ij} is the stress tensor that is mainly composed of thermoelasticity, ε_{kl} is the strain tensor, β_{kl} is the thermal expansion tensor, and ΔT is the laser-induced temperature change. Considering the monochromatic plane wave propagating along the surface normal direction in the monoclinic thin film, all the partial differentials of u_i along r_1 (x) and r_2 (y) equal 0 (see Section 10 of the Supporting Information for details). We can see that there is no external driving force for u_1 , while the nonzero off-diagonal term of elastic modules and thermal expansion coefficient (TEC) provides the external force that can drive both u_2 and u_3 oscillations. So the acoustic shear wave can, in principle, be excited in any monoclinic system. Qian et al.²⁰ reported two frequency oscillations in GaTe revealed by ultrafast electron diffraction; the low frequency, which was not explained clearly, is very likely the shear mode as predicted by the above equation. However, the excited acoustic shear modes are not guaranteed to be detectable, which still depend critically on the material properties, particularly the magnitudes of the nonzero off-diagonal terms of the elastic moduli and TEC. Furthermore, in low-symmetry systems, detected acoustic shear waves may arise not solely from thermoelastic effects but also involve nonthermal mechanisms, such as inverse piezoelectric effects in BiFeO₃⁶⁶ or ultrafast demagnetization in FePS₃.²⁷ Figure 6d,e displays the calculated atomic displacement in a 22 nm film at a pumping fluence of 1.3 mJ/cm². The results demonstrate that the external force generated

by thermal elastic stress can produce both commonly observed acoustic breathing phonons and unusual acoustic shear phonons. However, the amplitude of the shear phonon is about half the experimental value, indicating that other driving forces should be involved in the generation of the acoustic phonon. Recent studies have demonstrated the existence of a ferroelectric phase in Td-MoTe₂,⁶⁷ and one ultrafast experiment reported the light-induced ultrafast ferroelectric ordering⁵⁹ in T'-MoTe₂, which is induced by photoexcited image potential state electrons. Meanwhile, in ferroelectric polarized materials, the anomalous response driven by electric fields of photocarriers (inverse piezoelectric effect) is a well-accepted mechanism for large-amplitude structural change under laser excitation.^{68,69} Therefore, based on the reorientation effect of dipoles in ferroelectric polarized materials, we reasonably speculate that, alongside the thermoelastic effect, the inverse piezoelectric effect contributed by the nonperpendicular weak covalent bond and laser-induced surface charge plays a significant role in the generation of coherent shear phonons.

CONCLUSIONS

In summary, we have investigated ultrafast laser-excited coherent phonons in distorted octahedral MoTe₂ by UEM, focusing on the dependence of phonon modes on the stacking order. Combining ultrafast SAED and DF imaging, we verified the existence of two types of crystal plane-related acoustic phonon modes in T'-MoTe₂. Along with the consistency between the acoustic velocity ratio and the oscillation frequency ratio of the two acoustic phonon modes, we identified them as the breathing mode and shear mode propagating along the surface normal direction, respectively. The temperature-dependent ultrafast SAED results verified the switching of the shear modes from a high-temperature acoustic phonon to a low-temperature optical phonon, regulated by the temperature-driven stacking order change. Both the acoustic and optical shear modes involve the interlayer movement along the monoclinic direction and were unified within the framework of the LCM. Through quantitative experimental measurement of strain wave amplitude and numerical simulation, we speculate that the laser-induced inverse piezoelectric effect originating from interlayer polarization bonds associated with the stacking sequence is an important driving force for the coherent shear phonon mode. Our experimental results not only demonstrate a paradigm that stacking sequences regulate coherent shear phonons and topological transitions but also provide an efficient method to characterize stacking sequence-related structural phase transitions in two-dimensional layered materials.

MATERIALS AND METHODS

Sample Preparation and Static Characterization. Bulk MoTe₂ crystals were purchased from HQ Graphene. The bc -plane cross-sectional sample was fabricated by using a FIB system (Helios NanoLab 600i DualBeam, FEI Inc.). The stacking order was observed from the atomically resolved imaging acquired with HAADF-STEM on an aberration-corrected TEM (ARM-200F, JEOL). The samples we used for the UEM experiments were mechanically exfoliated in-plane (ab -plane) thin flakes with a thickness of 20–30 nm via the conventional mechanical exfoliation technique, placed on 2000 mesh copper grid (areas #1, #2, and #4) or 30 nm-thick Si₃N₄ film (area #3). The thickness of the free-standing MoTe₂ flakes was determined by the electron energy loss spectroscopy (EELS) log-ratio method using a simulated inelastic mean free path⁷⁰ (IMFP) of \sim 74.4 nm for

a 200 keV electron beam. For the flake on the Si_3N_4 substrate, atomic force microscopy (AFM) was used to determine the thickness.

Temperature-dependent resistivity measurements were performed using a standard four-probe method in a commercial physical properties measurement system (PPMS-16, Quantum Design). Confocal micro-Raman measurements with a backscattering configuration were performed by using a Jobin Yvon HR-Evolution system with a 632.8 nm HeNe laser as the excitation source. An attoDRY2100 closed-cycle cryostat was used to achieve temperature-dependent Raman measurement.

UEM Experiments. The ultrafast experiments were conducted at a new home-built ultrafast transmission electron microscope, which is a part of an ultrafast electron microscope station at the Synergetic Extreme Condition User Facility (SECUF). Figure 1e illustrates the schematic of the UEM based on the pump–probe technique. The UEM used in the experiments was modified based on a thermionic emission TEM (JEM-2100Plus, JEOL) with multiple imaging modes. The pump laser with a wavelength of 520 nm was employed to excite the sample by focusing it onto a spot with a full width at half-maximum (fwhm) diameter of ~ 40 μm . The probe laser with a wavelength of 260 nm was employed to excite the LaB_6 photocathode, thereby generating a photoelectron beam. The repetition rate for all the ultrafast measurements is set to 50 kHz. The pump and probe lasers are generated from a fundamental 1040 nm laser (Spirit1040–4, Spectra-Physics) with a pulse duration of 300 fs (fwhm) using a β -barium borate crystal. The time delay between them is regulated by controlling the optical path difference through a translation stage (DDS600, Thorlabs). The main experimental data in this study were collected at the selected-area electron diffraction (SAED) mode or the dark-field (DF) imaging mode. The in-plane information on the samples was obtained by incidence of the electron beam along the sample [001] direction. In order to obtain the out-of-plane information, the samples were tilted by 21° along the [011] direction (other tilt angle was also used), allowing for the diffraction pattern to contain information about the three crystal axes. The temperature-dependent experiments were performed using a double-tilt liquid nitrogen cooling sample holder (Model 636, Gatan). Unless otherwise stated, experiments were conducted at room temperature using a double-tilted or rotation sample holder.

Calculation Method. The Christoffel equation was used to determine the sound velocity and polarization vector of acoustic phonon modes propagating along the surface normal direction. The elastic modulus of $\text{T}'\text{-MoTe}_2$, which are the coefficients of the Christoffel equation, was adopted from the Supporting Information of ref 43 and checked by first-principles calculations. Due to the small value of C_{34} , the calculated LA mode and b -axis TA mode are almost independent. The elastic wave equation with laser-added external force (photothermo stress) was solved by the finite difference method to get the atomic displacement. To get the stress distribution along the sample slab depth, we solve the Maxwell equations in the $\text{T}'\text{-MoTe}_2$ thin film with boundary conditions. The specific values of the coefficients of the elastic wave equation used in the simulation can be found in Table S2, and the detailed calculation process can be found in Section 10 of the Supporting Information.

ASSOCIATED CONTENT

Supporting Information

The Supporting Information is available free of charge at <https://pubs.acs.org/doi/10.1021/acsnano.4c17877>.

Electron microscopy characterization of $\text{T}'\text{-MoTe}_2$ along the cross section; extended Raman spectroscopy data of bulk $\text{T}'\text{-MoTe}_2$; position and thickness of $\text{T}'\text{-MoTe}_2$ films; frequency ratio of acoustic phonons; pump-fluence dependence of coherent phonons; more details about ultrafast DF imaging and ultrafast SAED; more details about quantitative measurement of shear strain; softening of interlayer optical shear phonons; calculation of atomic displacement (PDF)

Time evolution of DF images selected from the $(\bar{1}22)$ diffraction peak (AVI)

Time evolution of DF images selected from the (150) diffraction peak (AVI)

Time evolution of DF images selected from the (200) diffraction peak (AVI)

Time evolution of DF images selected from the $(\bar{2}04)$ diffraction peak (AVI)

AUTHOR INFORMATION

Corresponding Authors

Shuaishuai Sun – Beijing National Laboratory for Condensed Matter Physics, Institute of Physics, Chinese Academy of Sciences, Beijing 100190, China; Songshan Lake Materials Laboratory, Dongguan, Guangdong 523808, China; orcid.org/0000-0002-9363-3901; Email: sss@iphy.ac.cn

Jianqi Li – Beijing National Laboratory for Condensed Matter Physics, Institute of Physics, Chinese Academy of Sciences, Beijing 100190, China; Songshan Lake Materials Laboratory, Dongguan, Guangdong 523808, China; School of Physical Sciences, University of Chinese Academy of Sciences, Beijing 100049, China; orcid.org/0000-0002-4808-6347; Email: ljq@iphy.ac.cn

Authors

Wenli Gao – Beijing National Laboratory for Condensed Matter Physics, Institute of Physics, Chinese Academy of Sciences, Beijing 100190, China; School of Physics, Northwest University, Xi'an 710069, China; orcid.org/0009-0005-4835-9121

Yongzhao Zhang – Institute of Quantum Materials and Physics, Henan Academy of Science, Zhengzhou 450046, China; orcid.org/0000-0003-4036-0900

Kaixin Zhu – Beijing National Laboratory for Condensed Matter Physics, Institute of Physics, Chinese Academy of Sciences, Beijing 100190, China; School of Physical Sciences, University of Chinese Academy of Sciences, Beijing 100049, China; orcid.org/0009-0008-8493-0067

Wentao Wang – Beijing National Laboratory for Condensed Matter Physics, Institute of Physics, Chinese Academy of Sciences, Beijing 100190, China; School of Physical Sciences, University of Chinese Academy of Sciences, Beijing 100049, China; orcid.org/0009-0002-2071-2390

Dong Yang – Beijing National Laboratory for Condensed Matter Physics, Institute of Physics, Chinese Academy of Sciences, Beijing 100190, China; School of Physical Sciences, University of Chinese Academy of Sciences, Beijing 100049, China; orcid.org/0009-0007-1931-6987

Jun Li – Beijing National Laboratory for Condensed Matter Physics, Institute of Physics, Chinese Academy of Sciences, Beijing 100190, China

Huanfang Tian – Beijing National Laboratory for Condensed Matter Physics, Institute of Physics, Chinese Academy of Sciences, Beijing 100190, China

Huaxin Yang – Beijing National Laboratory for Condensed Matter Physics, Institute of Physics, Chinese Academy of Sciences, Beijing 100190, China; School of Physical Sciences, University of Chinese Academy of Sciences, Beijing 100049, China; orcid.org/0000-0002-7857-2442

Xinghua Li – School of Physics, Northwest University, Xi'an 710069, China

Complete contact information is available at:

<https://pubs.acs.org/10.1021/acsnano.4c17877>

Author Contributions

J.Q.L. and S.S. conceived the project and supervised work. W.G. and S.S. designed the experiments. W.G. executed the experiments with help from S.S., K.Z., W.W., and D.Y. S.S. performed the data analysis and provided the calculation model for atomic displacements. W.G. processed the data and performed the atomic displacement simulations, the initial program was provided by Y.Z. W.G. and S.S. cowrote the paper. J.L. provided critical feedback on the paper. All authors contributed to the general discussion and commented on the manuscript.

Notes

The authors declare no competing financial interest.

ACKNOWLEDGMENTS

The authors thank Wenbo Sang for Raman experiments, Dacheng Tian for AFM measurements, Junqing Guo for preparing the sample on Si_3N_4 window, as well as Prof. Faran Zhou and Prof. Feng Jin for valuable discussions. This work was supported by the National Natural Science Foundation of China (grant no. U22A6005), the National Key R & D Program of China (grant nos. 2021YFA13011502, 2024YFA1408701, 2024YFA1408403, and 2024YFA1611303), the Scientific Instrument Developing Project of the Chinese Academy of Sciences (grant no. YJKYYQ20200055), and the Synergetic Extreme Condition User Facility (SECUF, <https://cstr.cn/31123.02.SECUF>).

REFERENCES

- (1) Hart, J. L.; Bhatt, L.; Zhu, Y.; Han, M.-G.; Bianco, E.; Li, S.; Hynke, D. J.; Schneeloch, J. A.; Tao, Y.; Louca, D.; Guo, P.; Zhu, Y.; Jornada, F.; Reed, E. J.; Kourkoutis, L. F.; Cha, J. J. Emergent layer stacking arrangements in c-axis confined MoTe_2 . *Nat. Commun.* **2023**, *14*, 4803.
- (2) Vizner Stern, M.; Salleh Atri, S.; Ben Shalom, M. Sliding van der Waals Polytypes. *Nat. Rev. Phys.* **2025**, *7*, 50–61.
- (3) Cao, Y.; Fatemi, V.; Fang, S.; Watanabe, K.; Taniguchi, T.; Kaxiras, E.; Jarillo-Herrero, P. Unconventional Superconductivity in Magic-Angle Graphene Superlattices. *Nature* **2018**, *556*, 43–50.
- (4) Song, T.; Fei, Z.; Yankowitz, M.; Lin, Z.; Jiang, Q.; Hwangbo, K.; Zhang, Q.; Sun, B.; Taniguchi, T.; Watanabe, K.; McGuire, M. A.; Graf, D.; Cao, T.; Chu, J.-H.; Cobden, D. H.; Dean, C. R.; Xiao, D.; Xu, X. Switching 2D Magnetic States via Pressure Tuning of Layer Stacking. *Nat. Mater.* **2019**, *18*, 1298–1302.
- (5) Vizner Stern, M.; Waschitz, Y.; Cao, W.; Nevo, I.; Watanabe, K.; Taniguchi, T.; Sela, E.; Urbakh, M.; Hod, O.; Ben Shalom, M. Interfacial Ferroelectricity by van der Waals sliding. *Science* **2021**, *372*, 1462–1466.
- (6) Yasuda, K.; Wang, X.; Watanabe, K.; Taniguchi, T.; Jarillo-Herrero, P. Stacking-Engineered Ferroelectricity in Bilayer Boron Nitride. *Science* **2021**, *372*, 1458–1462.
- (7) Liu, J.; Wang, H.; Fang, C.; Fu, L.; Qian, X. van der Waals Stacking-Induced Topological Phase Transition in Layered Ternary Transition Metal Chalcogenides. *Nano Lett.* **2017**, *17*, 467–475.
- (8) Li, Y.; Jia, Y.; Zhao, B.; Bao, H.; Huan, H.; Weng, H.; Yang, Z. Stacking-Layer-Tuned Topological Phases in $\text{M}_2\text{Bi}_2\text{Te}_3$ ($\text{M} = \text{Ge}, \text{Sn}, \text{Pb}$) Films. *Phys. Rev. B* **2023**, *108*, No. 085428.
- (9) Ji, S. Z.; Grånäs, O.; Weissenrieder, J. Manipulation of Stacking Order in Td-WTe₂ by Ultrafast Optical Excitation. *ACS Nano* **2021**, *15*, 8826–8835.
- (10) Liu, J.; Liu, P.; Yang, L.; Lee, S.-H.; Pan, M.; Chen, F.; Huang, J.; Jiang, B.; Hu, M.; Zhang, Y.; Xie, Z.; Wang, G.; Guan, M.; Jiang, W.; Yang, H.; Li, J.; Yun, C.; Wang, Z.; Meng, S.; Yao,

Y. et al. Nonvolatile Optical Control of Interlayer Stacking Order in 1T-TaS₂. 2024, 2405.02831. arXiv. <https://arxiv.org/abs/2405.02831>

- (11) Jiang, L.; Wang, S.; Shi, Z.; Jin, C.; Utama, M. I. B.; Zhao, S.; Shen, Y.-R.; Gao, H.-J.; Zhang, G.; Wang, F. Manipulation of Domain-Wall Solitons in Bi- and Trilayer Graphene. *Nat. Nanotechnol.* **2018**, *13*, 204–208.
- (12) Ruello, P.; Gusev, V. E. Physical Mechanisms of Coherent Acoustic Phonons Generation by Ultrafast Laser Action. *Ultrasonics* **2015**, *56*, 21–35.
- (13) Dhar, L.; Rogers, J. A.; Nelson, K. A. Time-Resolved Vibrational Spectroscopy in the Impulsive Limit. *Chem. Rev.* **1994**, *94*, 157–193.
- (14) Violla, F.; Fatti, N. D. Time-Domain Investigations of Coherent Phonons in van der Waals Thin Films. *Nanomaterials* **2020**, *10*, 2543.
- (15) Sie, E. J.; Nyby, C. M.; Pemmaraju, C. D.; Park, S. J.; Shen, X. Z.; Yang, J.; Hoffmann, M. C.; Ofori-Okai, B. K.; Li, R. K.; Reid, A. H.; Weathersby, S.; Mannebach, E.; Finney, N.; Rhodes, D.; Chenet, D.; Antony, A.; Balicas, L.; Hone, J.; Devereaux, T. P.; Heinz, T. F.; et al. An Ultrafast Symmetry Switch in a Weyl Semimetal. *Nature* **2019**, *565*, 61–66.
- (16) Chen, S.-Y.; Goldstein, T.; Venkataraman, D.; Ramasubramanian, A.; Yan, J. Activation of New Raman Modes by Inversion Symmetry Breaking in Type II Weyl Semimetal Candidate T'-MoTe₂. *Nano Lett.* **2016**, *16*, 5852–5860.
- (17) Zhao, Y.; Luo, X.; Li, H.; Zhang, J.; Araujo, P. T.; Gan, C. K.; Wu, J.; Zhang, H.; Quek, S. Y.; Dresselhaus, M. S.; Xiong, Q. Interlayer Breathing and Shear Modes in Few-Trilayer MoS₂ and WSe₂. *Nano Lett.* **2013**, *13*, 1007–1015.
- (18) Zhou, F. R.; Liu, H. H.; Zajac, M.; Hwangbo, K.; Jiang, Q. N.; Chu, J. H.; Xu, X. D.; Arslan, I.; Gage, T. E.; Wen, H. D. Ultrafast Nanoimaging of Spin-Mediated Shear Waves in an Acoustic Cavity. *Nano Lett.* **2023**, *23*, 10213–10220.
- (19) Lee, M. C.; Sirica, N.; Teitelbaum, S. W.; Maznev, A.; Pezeril, T.; Tutchtton, R.; Kravivin, V.; de la Pena, G. A.; Huang, Y.; Zhao, L. X.; Chen, G. F.; Xu, B.; Yang, R.; Shi, J.; Zhu, J. X.; Yarotski, D. A.; Qiu, X. G.; Nelson, K. A.; Trigo, M.; Reis, D. A.; et al. Direct Observation of Coherent Longitudinal and Shear Acoustic Phonons in TaAs Using Ultrafast X-Ray Diffraction. *Phys. Rev. Lett.* **2022**, *128*, No. 155301.
- (20) Qian, Q.; Shen, X.; Luo, D.; Jia, L.; Kozina, M.; Li, R.; Lin, M.-F.; Reid, A. H.; Weathersby, S.; Park, S.; Yang, J.; Zhou, Y.; Zhang, K.; Wang, X.; Huang, S. Coherent Lattice Wobbling and Out-of-Phase Intensity Oscillations of Friedel Pairs Observed by Ultrafast Electron Diffraction. *ACS Nano* **2020**, *14*, 8449–8458.
- (21) Rivas, N.; Zhong, S.; Dekker, T.; Cheng, M.; Gicala, P.; Chen, F.; Luo, X.; Sun, Y.; Petruk, A. A.; Pichugin, K.; Tsen, A. W.; Sciaini, G. Generation and detection of coherent longitudinal acoustic waves in ultrathin 1T'-MoTe₂. *Appl. Phys. Lett.* **2019**, *115*, No. 223103.
- (22) Lui, C. H.; Malard, L. M.; Kim, S.; Lantz, G.; Laverge, F. E.; Saito, R.; Heinz, T. F. Observation of Layer-Breathing Mode Vibrations in Few-Layer Graphene through Combination Raman Scattering. *Nano Lett.* **2012**, *12*, 5539–5544.
- (23) Tan, P. H.; Han, W. P.; Zhao, W. J.; Wu, Z. H.; Chang, K.; Wang, H.; Wang, Y. F.; Bonini, N.; Marzari, N.; Pugno, N.; Savini, G.; Lombardo, A.; Ferrari, A. C. The Shear Mode of Multilayer Graphene. *Nat. Mater.* **2012**, *11*, 294–300.
- (24) Mannebach, E. M.; Nyby, C.; Ernst, F.; Zhou, Y.; Tolsma, J.; Li, Y.; Sher, M.-J.; Tung, I. C.; Zhou, H.; Zhang, Q.; Seyler, K. L.; Clark, G.; Lin, Y.; Zhu, D.; Glownia, J. M.; Kozina, M. E.; Song, S.; Nelson, S.; Mehta, A.; Yu, Y.; et al. Dynamic Optical Tuning of Interlayer Interactions in the Transition Metal Dichalcogenides. *Nano Lett.* **2017**, *17*, 7761–7766.
- (25) Park, H. S.; Baskin, J. S.; Barwick, B.; Kwon, O.-H.; Zewail, A. H. 4D Ultrafast Electron Microscopy: Imaging of Atomic Motions, Acoustic Resonances, and Moiré Fringe Dynamics. *Ultramicroscopy* **2009**, *110*, 7–19.
- (26) Zhang, Y. Z.; Sun, S. S.; Wang, W. T.; Tian, H. F.; Li, J. Q.; Li, J.; Yang, H. X. Inhomogeneous Excitation-Regulated Coherent Strain Wave in 2H-MoTe₂ Revealed by Ultrafast Electron Microscopy. *Phys. Rev. B* **2023**, *108*, No. 245426.

- (27) Zong, A. L.; Zhang, Q.; Zhou, F. R.; Su, Y. F.; Hwangbo, K.; Shen, X. Z.; Jiang, Q. N.; Liu, H. H.; Gage, T. E.; Walko, D. A.; Kozina, M. E.; Luo, D.; Reid, A. H.; Yang, J.; Park, S.; Lapidus, S. H.; Chu, J. H.; Arslan, I.; Wang, X. J.; Xiao, D.; et al. Spin-Mediated Shear Oscillators in a Van Der Waals Antiferromagnet. *Nature* **2023**, *620*, 988–993.
- (28) Lejman, M.; Vaudel, G.; Infante, I. C.; Gemeiner, P.; Gusev, V. E.; Dkhil, B.; Ruello, P. Giant Ultrafast Photo-Induced Shear Strain in Ferroelectric BiFeO₃. *Nat. Commun.* **2014**, *5*, 4301.
- (29) Fang, S.; Duan, S.; Wang, X.; Chen, S.; Li, L.; Li, H.; Jiang, B.; Liu, C.; Wang, N.; Zhang, L.; Wen, X.; Yao, Y.; Zhang, J.; Xie, D.; Luo, Y.; Xu, W. Direct Characterization of Shear Phonons in Layered Materials by Mechano-Raman Spectroscopy. *Nat. Photonics* **2023**, *17*, 531–537.
- (30) Qi, Y. P.; Naumov, P. G.; Ali, M. N.; Rajamathi, C. R.; Schnelle, W.; Barkalov, O.; Hanfland, M.; Wu, S. C.; Shekhar, C.; Sun, Y.; Süß, V.; Schmidt, M.; Schwarz, U.; Pippel, E.; Werner, P.; Hillebrand, R.; Förster, T.; Kampert, E.; Parkin, S.; Cava, R. J.; et al. Superconductivity in Weyl semimetal candidate MoTe₂. *Nat. Commun.* **2016**, *7*, 11038.
- (31) Berger, A. N.; Andrade, E.; Kerelsky, A.; Edelberg, D.; Li, J.; Wang, Z.; Zhang, L.; Kim, J.; Zaki, N.; Avila, J.; Chen, C.; Asensio, M. C.; Cheong, S.-W.; Bernevig, B. A.; Pasupathy, A. N. Temperature-driven topological transition in 1T'-MoTe₂. *npj Quantum Mater.* **2018**, *3*, 2.
- (32) Zhang, M. Y.; Wang, Z. X.; Li, Y. N.; Shi, L. Y.; Wu, D.; Lin, T.; Zhang, S. J.; Liu, Y. Q.; Liu, Q. M.; Wang, J.; Dong, T.; Wang, N. L. Light-Induced Subpicosecond Lattice Symmetry Switch in MoTe₂. *Phys. Rev. X* **2019**, *9*, No. 021036.
- (33) Qi, Y. P.; Guan, M. X.; Zahn, D.; Vasileiadis, T.; Seiler, H.; Windsor, Y. W.; Zhao, H.; Meng, S.; Ernstorfer, R. Traversing Double-Well Potential Energy Surfaces: Photoinduced Concurrent Intralayer and Interlayer Structural Transitions in XTe₂ (X = Mo, W). *ACS Nano* **2022**, *16*, 11124–11135.
- (34) Ji, S.; Grånäs, O.; Kumar Prasad, A.; Weissenrieder, J. Influence of strain on an ultrafast phase transition. *Nanoscale* **2022**, *15*, 304–312.
- (35) Huang, F.-T.; Joon Lim, S.; Singh, S.; Kim, J.; Zhang, L.; Kim, J.-W.; Chu, M.-W.; Rabe, K. M.; Vanderbilt, D.; Cheong, S.-W. Polar and phase domain walls with conducting interfacial states in a Weyl semimetal MoTe₂. *Nat. Commun.* **2019**, *10*, 4211.
- (36) Cao, C. W.; Liu, X.; Ren, X.; Zeng, X. Z.; Zhang, K. N.; Sun, D.; Zhou, S. Y.; Wu, Y.; Li, Y.; Chen, J. H. Barkhausen Effect in the First Order Structural Phase Transition in Type-II Weyl Semimetal MoTe₂. *2D Mater.* **2018**, *5*, 044003.
- (37) Cheon, Y.; Lim, S. Y.; Kim, K.; Cheong, H. Structural Phase Transition and Interlayer Coupling in Few-Layer 1T' and Td MoTe₂. *ACS Nano* **2021**, *15*, 2962–2970.
- (38) Deng, Y.; Zhao, X.; Zhu, C.; Li, P.; Duan, R.; Liu, G.; Liu, Z. MoTe₂: Semiconductor or Semimetal? *ACS Nano* **2021**, *15*, 12465–12474.
- (39) Clarke, R.; Marseglia, E.; Hughes, H. P. A Low-Temperature Structural Phase Transition in β -MoTe₂. *Philos. Mag. B* **1978**, *38*, 121–126.
- (40) Kim, S.; Kim, Y.; Kim, J.; Choi, S.; Yun, K.; Kim, D.; Lim, S. Y.; Kim, S.; Chun, S. H.; Park, J.; Eom, I.; Kim, K. S.; Koo, T.-Y.; Ou, Y.; Katmis, F.; Wen, H.; DiChiara, A.; Walko, D. A.; Landahl, E. C.; Cheong, H.; et al. Ultrafast Carrier–Lattice Interactions and Interlayer Modulations of Bi₂Se₃ by X-ray Free-Electron Laser Diffraction. *Nano Lett.* **2021**, *21*, 8554–8562.
- (41) Zhao, Y.; Luo, X.; Zhang, J.; Wu, J.; Bai, X.; Wang, M.; Jia, J.; Peng, H.; Liu, Z.; Quek, S. Y.; Xiong, Q. Interlayer Vibrational Modes in Few-Quintuple-Layer Bi₂Te₃ and Bi₂Se₃ Two-Dimensional Crystals: Raman Spectroscopy and First-Principles Studies. *Phys. Rev. B* **2014**, *90*, No. 245428.
- (42) Blakslee, O. L.; Proctor, D. G.; Seldin, E. J.; Spence, G. B.; Weng, T. Elastic Constants of Compression-Annealed Pyrolytic Graphite. *J. Appl. Phys.* **1970**, *41*, 3373–3382.
- (43) Singh, S.; Kim, J.; Rabe, K. M.; Vanderbilt, D. Engineering Weyl Phases and Nonlinear Hall Effects in Td-MoTe₂. *Phys. Rev. Lett.* **2020**, *125*, No. 046402.
- (44) Nakamura, A.; Shimojima, T.; Chiashi, Y.; Kamitani, M.; Sakai, H.; Ishiwata, S.; Li, H.; Ishizaka, K. Nanoscale Imaging of Unusual Photoacoustic Waves in Thin Flake VTe₂. *Nano Lett.* **2020**, *20*, 4932–4938.
- (45) Li, J. J.; Chen, J.; Reis, D. A.; Fahy, S.; Merlin, R. Optical Probing of Ultrafast Electronic Decay in Bi and Sb with Slow Phonons. *Phys. Rev. Lett.* **2013**, *110*, No. 047401.
- (46) Zhang, K.; Bao, C.; Gu, Q.; Ren, X.; Zhang, H.; Deng, K.; Wu, Y.; Li, Y.; Feng, J.; Zhou, S. Raman signatures of inversion symmetry breaking and structural phase transition in type-II Weyl semimetal MoTe₂. *Nat. Commun.* **2016**, *7*, 13552.
- (47) Zeiger, H. J.; Vidal, J.; Cheng, T. K.; Ippen, E. P.; Dresselhaus, G.; Dresselhaus, M. S. Theory for Displacive Excitation of Coherent Phonons. *Phys. Rev. B* **1992**, *45*, 768–778.
- (48) Kim, Y.-J.; Lee, Y.; Kim, K.; Kwon, O.-H. Light-Induced Anisotropic Morphological Dynamics of Black Phosphorus Membranes Visualized by Dark-Field Ultrafast Electron Microscopy. *ACS Nano* **2020**, *14*, 11383–11393.
- (49) Cremons, D. R.; Plemmons, D. A.; Flannigan, D. J. Femtosecond electron imaging of defect-modulated phonon dynamics. *Nat. Commun.* **2016**, *7*, 11230.
- (50) Cremons, D. R.; Plemmons, D. A.; Flannigan, D. J. Defect-mediated phonon dynamics in TaS₂ and WSe₂. *Struct. Dyn.* **2017**, *4*, No. 044019.
- (51) Zhang, Y.; Flannigan, D. J. Observation of Anisotropic Strain-Wave Dynamics and Few-Layer Dephasing in MoS₂ with Ultrafast Electron Microscopy. *Nano Lett.* **2019**, *19*, 8216–8224.
- (52) Tong, L.; Yuan, J.; Zhang, Z.; Tang, J.; Wang, Z. Nanoscale Subparticle Imaging of Vibrational Dynamics using Dark-Field Ultrafast Transmission Electron Microscopy. *Nat. Nanotechnol.* **2023**, *18*, 145–152.
- (53) Danz, T.; Domröse, T.; Ropers, C. Ultrafast Nanoimaging of the Order Parameter in a Structural Phase Transition. *Science* **2021**, *371*, 371–374.
- (54) Zhang, Y.; Flannigan, D. J. Imaging Nanometer Phonon Softening at Crystal Surface Steps with 4D Ultrafast Electron Microscopy. *Nano Lett.* **2021**, *21*, 7332–7338.
- (55) Zhang, Y.; Li, J.; Wang, W.; Tian, H.; Gao, W.; Li, J.; Sun, S.; Yang, H. Simulation of ultrafast electron diffraction intensity under coherent acoustic phonons. *Struct. Dyn.* **2023**, *10*, No. 064102.
- (56) He, B.; Zhang, C.; Zhu, W.; Li, Y.; Liu, S.; Zhu, X.; Wu, X.; Wang, X.; Wen, H.-H.; Xiao, M. Coherent optical phonon oscillation and possible electronic softening in WTe₂ crystals. *Sci. Rep.* **2016**, *6*, 30487.
- (57) Liang, L.; Puretzy, A. A.; Sumpter, B. G.; Meunier, V. Interlayer Bond Polarizability Model for Stacking-Dependent Low-Frequency Raman Scattering in Layered Materials. *Nanoscale* **2017**, *9*, 15340–15355.
- (58) Luo, X.; Lu, X.; Cong, C.; Yu, T.; Xiong, Q.; Quek, S. Y. Stacking sequence determines Raman intensities of observed interlayer shear modes in 2D layered materials – A general bond polarizability model. *Sci. Rep.* **2015**, *5*, 14565.
- (59) Dai, Y.; Zheng, Q.; Ziffer, M. E.; Rhodes, D.; Hone, J.; Zhao, J.; Zhu, X. Ultrafast Ferroelectric Ordering on the Surface of a Topological Semimetal MoTe₂. *Nano Lett.* **2021**, *21*, 9903–9908.
- (60) Han, X.; Liang, X.; He, D.; Jiao, L.; Wang, Y.; Zhao, H. Photocarrier Dynamics in MoTe₂ Nanofilms with 2H and Distorted 1T Lattice Structures. *ACS Appl. Mater. Interfaces* **2021**, *13*, 44703–44710.
- (61) Hu, X.; Zhang, F.; Hu, Z.; He, P.; Tao, L.; Zheng, Z.; Zhao, Y.; Yang, Y.; He, J. Preparation of 1T' and 2H-MoTe₂ Films and Investigation of Their Photoelectric Properties and Ultrafast Photocarrier Dynamics. *Opt. Mater.* **2023**, *136*, No. 113467.
- (62) Yang, Q.; Wu, M.; Li, J. Origin of Two-Dimensional Vertical Ferroelectricity in WTe₂ Bilayer and Multilayer. *J. Phys. Chem. Lett.* **2018**, *9*, 7160–7164.

(63) Wan, Y.; Hu, T.; Mao, X.; Fu, J.; Yuan, K.; Song, Y.; Gan, X.; Xu, X.; Xue, M.; Cheng, X.; Huang, C.; Yang, J.; Dai, L.; Zeng, H.; Kan, E. Room-Temperature Ferroelectricity in 1T'-ReS₂ Multilayers. *Phys. Rev. Lett.* **2022**, *128*, No. 067601.

(64) Xiao, J.; Wang, Y.; Wang, H.; Pemmaraju, C. D.; Wang, S.; Muscher, P.; Sie, E. J.; Nyby, C. M.; Devereaux, T. P.; Qian, X.; Zhang, X.; Lindenberg, A. M. Berry Curvature Memory Through Electrically Driven Stacking Transitions. *Nat. Phys.* **2020**, *16*, 1028–1034.

(65) Park, J.; Yeu, I. W.; Han, G.; Hwang, C. S.; Choi, J.-H. Ferroelectric switching in bilayer 3R MoS₂ via interlayer shear mode driven by nonlinear phononics. *Sci. Rep.* **2019**, *9*, 14919.

(66) Juvé, V.; Gu, R.; Gable, S.; Maroutian, T.; Vaudel, G.; Matzen, S.; Chigarev, N.; Raetz, S.; Gusev, V. E.; Viret, M.; Jarnac, A.; Laulhé, C.; Maznev, A. A.; Dkhil, B.; Ruello, P. Ultrafast Light-Induced Shear Strain Probed by Time-Resolved X-ray Diffraction: Multiferroic BiFeO₃ as a Case Study. *Phys. Rev. B* **2020**, *102*, No. 220303.

(67) Jindal, A.; Saha, A.; Li, Z.; Taniguchi, T.; Watanabe, K.; Hone, J. C.; Birol, T.; Fernandes, R. M.; Dean, C. R.; Pasupathy, A. N.; Rhodes, D. A. Coupled Ferroelectricity and Superconductivity in Bilayer Td-MoTe₂. *Nature* **2023**, *613*, 48–52.

(68) Gu, R.; Juvé, V.; Laulhé, C.; Bouyanfif, H.; Vaudel, G.; Poirier, A.; Dkhil, B.; Hollander, P.; Paillard, C.; Weber, M. C.; Sando, D.; Fusil, S.; Garcia, V.; Ruello, P. Temporal and spatial tracking of ultrafast light-induced strain and polarization modulation in a ferroelectric thin film. *Sci. Adv.* **2023**, *9*, No. ead11160.

(69) Wen, H.; Chen, P.; Cosgriff, M. P.; Walko, D. A.; Lee, J. H.; Adamo, C.; Schaller, R. D.; Ihlefeld, J. F.; Dufresne, E. M.; Schlom, D. G.; Evans, P. G.; Freeland, J. W.; Li, Y. Electronic Origin of Ultrafast Photoinduced Strain in BiFeO₃. *Phys. Rev. Lett.* **2013**, *110*, No. 037601.

(70) Malis, T.; Cheng, S. C.; Egerton, R. F. EELS Log-Ratio Technique for Specimen-Thickness Measurement in the TEM. *J. Electron Microsc. Technol.* **1988**, *8*, 193–200.